Electron Temperature Measurements of Solid Density Plasmas Produced by Intense Ultrashort Laser Pulses

G. Guethlein, M. E. Foord, and D. Price

Lawrence Livermore National Laboratory, University of California, P.O. Box 808, Livermore, California 94550

(Received 26 February 1996)

We report the first spatially and temporally localized measurements of 500 eV electron temperatures in solid density Al plasmas generated by a 3×10^{17} W/cm^2, 170 fs laser. Expansion velocities of marker layers from various depths are sampled with mass-resolved ion time-of-flight spectroscopy. Hydrodynamic simulations relate the measured velocities to the sound speed, determining the temperature along the central axis of the plasma. Results are consistent with conductive heating of the first 1000 Å. [S0031-9007(96)00721-1]

PACS numbers: 52.70.Nc, 52.40.Nk, 52.50.Jm, 52.65.Kj

Recent advances in high intensity sub-ps laser technology have allowed new regimes of hot dense matter to be investigated [1–6]. Plasmas in the kilovolt temperature range at near solid densities are relevant to areas such as intense x-ray source development [6] and for inertial confinement fusion applications [7]. The macroscopic properties of these plasmas are determined by complex interactions such as laser absorption mechanisms at high intensities [4,5], and the generation and transport of radiation [8–10] and particle fluxes [11–14].

Dense, high temperature plasmas are typically studied by x-ray spectroscopy, particle emission, and Doppler shift spectroscopy. Ion time-of-flight (TOF) measurements have been used previously to determine suprathermal electron temperatures of plasmas produced by lasers with pulse lengths from 1 ps [15] to 1 ns [16]. Ion energy distributions with MeV proton energies have recently been reported from 3 ps laser pulses [17]. Spatially and temporally averaged x-ray spectra of sub-ps laser produced plasmas have shown electron temperatures of a few hundred eV [9,10]. However, determining the peak temperature from x-ray spectra is problematic, since the fastest reported x-ray streak camera response is 0.89 ps [18], while simulations presented here indicate cooling times of a few hundred femtoseconds. Attenuation of cold $K\alpha$ emission with depth in the target has been used to measure the suprathermal electron temperature [13,14] but does not measure the thermal electron temperature. Doppler shift measurements have been used to determine temperatures at lower intensities [19,20] but interpretation requires the inclusion of ponderomotive effects above 10^{17} W/cm^2 [21].

For sub-ps laser heating, solid density plasmas are produced with scale lengths shorter than the laser wavelength. Hydrodynamic expansion of such plasmas should be relatively simple to measure and interpret theoretically. Ions from the surface expand during the laser pulse, and therefore are driven by an electron distribution which may contain a suprathermal component. For the plasma conditions of this Letter, expansion from depths greater than ~100 Å occurs after the laser pulse, and therefore is driven only by thermal electron pressure. Thus, expansion velocities from surface and embedded materials are indicative of suprathermal and thermal temperatures, respectively. The work presented in this Letter is novel in that embedded layers are used to mark the plasma expansion as a function of depth in the target. Expansion velocity measurements are then related by the hydrodynamic code LASNEX [22] to the local temporal peak of the electron temperature, as a function of depth. Each local temporal temperature peak occurs as the heat wave propagates through that location. By observing ion velocities from the central axis of the expansion, only the plasma heated by the spatial peak of the intensity profile is sampled, providing effective spatial isolation. Thus, we believe these to be the first measurements that sample both the spatial and temporal peak of the thermal electron temperature.

The experiments were conducted at the Lawrence Livermore National Laboratory Ultra Short Pulse Laser Facility. The laser utilized chirped pulse amplification in Ti:Sapphire [23,24]. The 170 fs, 800 nm laser pulses were frequency doubled to provide an intensity contrast greater than 10^7, at 1 ps before the peak of the 400 nm pulse [5]. With a FWHM (Gaussian fit) focal spot of 3 μm and an energy delivered to the target of 6 mJ, the peak intensity obtained was 3×10^{17} W/cm^2. The targets were electron-beam deposited films on Kodak projector slide cover glass. The base layer was 1 μm of aluminum. This was overcoated with 100 Å of MgF_2. The final layer was comprised of aluminum stripes of thickness from 100 to 5000 Å. All data were collected with the same laser operating conditions and without breaking vacuum. The laser energy and pulse width typically varied by less than 10% shot to shot. The laser was incident at 22°, allowing ions to be collected normal to the target. The *S*-polarization data presented here were slightly elliptical, due to a mismatched wave plate.

Performance of the magnetically separated ion time of flight spectrometer has been described elsewhere [25]. Ions enter through a 250 μm slit (59 cm from the target) and are deflected by an electromagnet before striking

a microchannel plate detector (70 cm from the target) coupled to an optical streak camera. The signature of each ionic species is a straight line on the streak camera image. A typical image with a 100 Å thick MgF_2 marker layer embedded at 500 Å is shown in Fig. 1. Note the presence of protons and carbon ions resulting from hydrocarbon contamination of the target surface. Ion separation by charge to mass ratio allows observation of the flight time from the marker layer. The instrument sensitivity is sufficient to easily observe 100 Å thick marker layers, even 5000 Å into the target. For subsequent discussion, ions will be considered as coming from the middle of a marker layer and the time of flight as the average for that layer.

Plotted in Fig. 2 are ion TOF speeds as a function of marker depth, for both *P* and *S* polarization. Each point averages three to five measurements taken at a peak laser intensity of 3×10^{17} W/cm^2, with the error bars representing the overall scatter in the data. The velocities decrease with depth roughly as $d^{-1/2}$. The *P*-polarized velocities are ~25% higher than the *S*-polarized data. The results are compared with simulations below.

The laser absorption and hydrodynamics are simulated using the LASNEX hydrodynamics code in one dimensional planar geometry. The Lagrangian mesh has sufficient resolution to resolve the laser absorption near the critical surface. The laser absorption is calculated by solving the Helmholtz wave equations [26] using the ac conductivity model described in Ref. [5]. Calculations are performed for both *S* and *P* linearly polarized light with an angle of incidence of 22°. In the case of *S*-polarized light, heating is due only to inverse bremsstrahlung. For *P* polarization, heating from resonant absorption is also included using a simple model that includes damping due to collisions, wave breaking, and Landau damping [26]. Ponderomotive effects that couple the laser field to the hydrodynamics are also included. A non-LTE (–local thermal equilibrium) time-dependent average-atom atomic model is used in the calculations to determine the average charge state and pressure in the plasma. A thermal flux limiter (FL) between one (as used in Ref. [5]) and 0.1 is applied.

The plasma expands normal to the target along the central axis, which passes through the center of the laser spot. Because of the laser intensity profile, the radial pressure gradient also drives a slight (relative to axial) radial expansion. As a result, only ions originating from the center of the laser spot would enter the detector, neglecting ion thermal motion. Preliminary 2D simulations indicate that the central 1 μm region expands into an ~5° cone. Because of expansion, the ion mean free path eventually exceeds the radial scale length. Ion thermal motion ($T_i < 5$ eV) then allows some radial mixing, and we estimate that ions originating within only 0.3 μm of the central axis can be detected. Thus, we sample only intensities within 3% of the peak. Also, the 2D simulations show only a (3–5)% decrease in velocities along the central axis as compared with 1D results. Therefore 1D simulations using the peak laser intensity should correctly model the ion TOF data in our geometry.

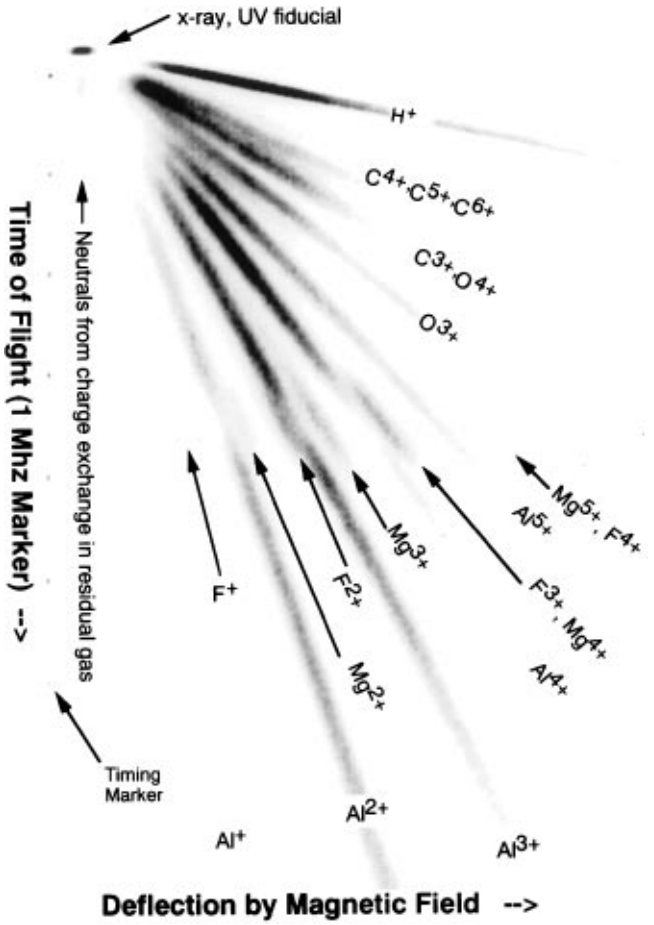

FIG. 1. Streak image from the ion time-of-flight spectrometer. The MgF_2 marker layer was embedded at 500 Å.

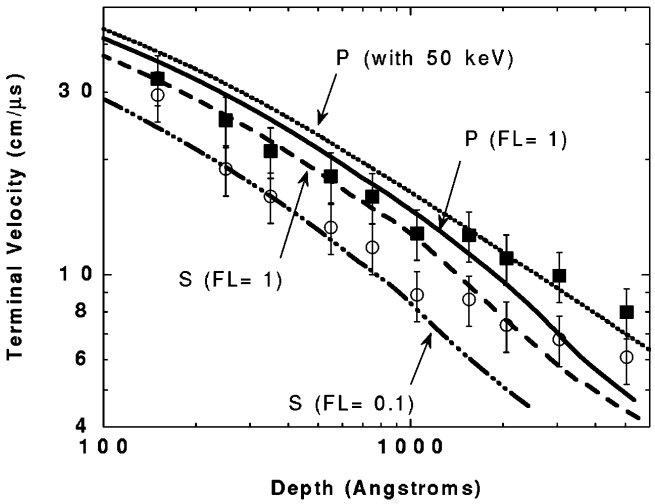

FIG. 2. Measured ion velocities and simulation results, for a peak laser intensity of 3×10^{17} W/cm^2. The solid squares and open circles are for *P* and *S* polarization, respectively. Simulation results are shown as curves.

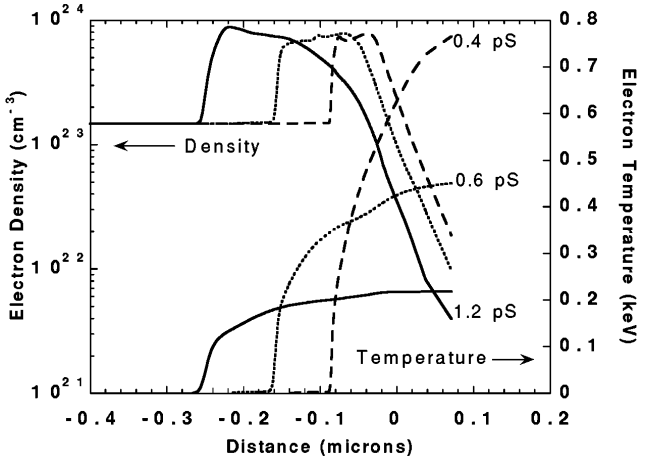

FIG. 3. LASNEX simulations of electron density and electron temperature at times of 0.4, 0.6, and 1.2 ps after the peak of laser pulse. The initial laser solid interface is at the origin and the laser ($I_{\text{peak}} = 3 \times 10^{17}$ W/cm^2) is incident from the right.

Shown in Fig. 3, for a peak laser intensity of 3×10^{17} W/cm^2, are 1D LASNEX calculations of electron density and temperature at three different times during the expansion. Electrons are cooled both by heat conduction into the target and by expansion. As the plasma expands, the electron thermal energy is converted to ion kinetic energy, and ions approach terminal velocity (v_{term}). Terminal velocities from the simulations are plotted in Fig. 2. Though we make no attempt here to optimize the flux limiter, it is apparent that for some value between 0.1 and 1, agreement can be found with the measured velocities, for depths $d < 1000$ Å. Larger depths and suprathermals will be discussed later. Note that the lower three curves (absorption into thermal electrons) have similar shapes, but shifted values. Value shifts result from differences in absorbed energy, with FL = 0.1 having a hotter absorption region, but lower overall absorption than FL = 1. The shape (or slope) is simply indicative of the energy transport into the target.

The slope with depth (d) of the calculated velocities may be understood from a simple scaling argument. As discussed below, $v_{\text{term}}(d) \propto c_{sp}(d)$, the peak sound speed at the time the heat wave reaches depth d in the target. Material near the surface is conductively heated before energy is transferred to hydrodynamic motion, so $T_e \propto E_0/d$ for times $t > \tau_{\text{laser}}$ (E_0 is the deposited laser energy and τ_{laser} is the pulse width of the laser). Since $c_{sp} \propto T_e^{1/2}$, we find $v_{\text{term}} \propto d^{-1/2}$. At larger depths, hydrodynamic energy is no longer negligible and the calculated velocities decrease more quickly with depth. The apparent agreement between the measured and calculated slopes for depths <1000 Å therefore indicates conductive heating of this region.

To determine the peak temperatures in the plasma, we first relate v_{term} to c_{sp}. For example, $v = 2c_{so}/(\gamma - 1)$ for semi-infinite expansion with initial sound speed c_{so} and adiabatic constant γ. However, for finite energy deposition on a semi-infinite surface, the temperature at the plasma-solid interface decreases in time during expansion due to energy transport into the cold material. Simulations show that $v_{\text{term}}/c_{sp} \sim 3$ near the surface, as would be expected for $\gamma = 5/3$, and that the ratio is closer to one for depths larger than $\sim c_{so}\tau_{\text{laser}}$. A simple analytic model derives a similar result and will be presented elsewhere [27]. Since $c_s = \sqrt{\gamma Z T_e/m_i}$, we find the temperature from

$$ZT_e = \frac{m_i}{\gamma(d)}\left(\frac{c_{sp}(d)}{v_{\text{term}}(d)}\right)^2 v_{\text{TOF}}^2, \qquad (1)$$

where v_{TOF} is the measured velocity, while γ and v_{term}/c_{sp} are calculated from simulations. We find, for depths between 100 and 1000 Å that $\gamma(v_{\text{term}}/c_{sp})^2$ is only weakly dependent upon plasma conditions, varying by less than $\pm 20\%$ through more than an order of magnitude in laser intensity and flux limiter. ZT_e calculated from Eq. (1) is thus relatively model independent. T_e is then found self-consistently using an ionization table (non-LTE, derived from the simulations).

Using Eq. (1) and the measured velocities from a peak laser intensity of 3×10^{17} W/cm^2, the peak electron temperatures are calculated and plotted in Fig. 4. From the uncertainty in $\gamma(v_{\text{term}}/c_{sp})^2$, and that in the measurements, we estimate a total uncertainty in the reduced temperature data of $\pm 36\%$. The electron temperature determined directly from LASNEX simulations is also shown in Fig. 4, showing similar values and depth dependence for depths less than 1000 Å. The mass density at the peak sound speed (and temperature) is also plotted. Ions nearest the vacuum-solid interface reach the highest temperature, but due to expansion achieve maximum temperature at less

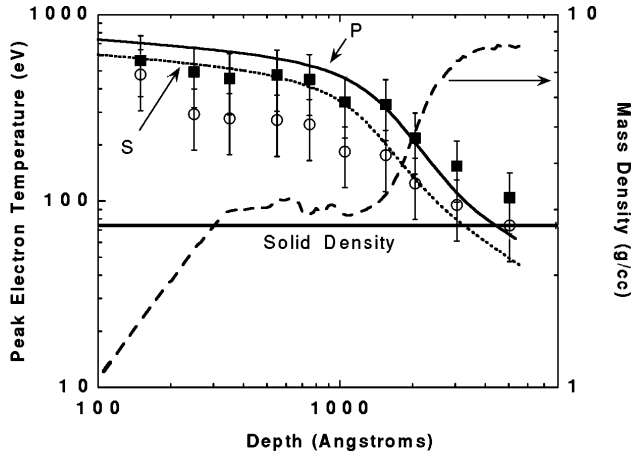

FIG. 4. Peak electron temperatures deduced from the experimental data of Fig. 2. The solid squares and open circles are for P and S polarization, respectively. Peak electron temperatures and mass density from simulations with FL = 1 are shown as curves. Peak laser intensity was 3×10^{17} W/cm^2 for both simulation and data.

than solid density. At 250 Å, near solid densities are achieved at temperatures of 500 eV. For material deeper than 1000 Å, a strong shock is evident and the density reaches a few times solid, as the temperature drops to near 100 eV. The electron temperatures near solid density are almost twice the temporal and spatially averaged values reported [12] for similar intensities and target materials.

Referring to Fig. 2, the calculated velocities quickly fall below the measurements for depths $d > 2000$ Å. The thermal conduction model used in the simulations [28] is generally less accurate in dense, lower temperature regimes and may be partially responsible for the discrepancy. Nonlocal transport models and calculations with small flux limiters decrease inward heat flow [29,30], and would worsen the discrepancy. Since the presence of suprathermal electrons is suggested by the observation of protons with energies of 100 and 50 keV, for *P* and *S* polarization, respectively, we consider the possibility that suprathermal electrons from the laser-surface interaction penetrate and heat the deeper regions, thus raising the velocities deep in the target. (The presence of high energy electrons in the *S* case is attributed to the equivalent intensity of 12% *P* from the wave-plate mismatch.) Full treatment of the laser-plasma interaction requires solution of the Fokker-Planck equations coupled to the laser field [31]. However, the effects of suprathermal electrons can be qualitatively calculated by adding a nonthermal electron component on the surface. Simulations were performed in which 3% of the laser energy (a 50% increase in absorption) was deposited into 50 keV electrons near the surface. The effect of suprathermals on v_{term} is due to preheating at large depths rather than a direct effect of the suprathermal pressure. We then find better agreement for depths >2000 Å.

In summary, measurements of the expansion velocities of marker layers have demonstrated the generation of 500 eV solid density plasmas. Our measurements provide both spatial and temporal localization of the thermal electron temperature. For $d < 1000$ Å agreement between the *slope* of ion velocity and the simulation results suggests that conduction dominates the heat flow in this region, and the velocities and electron temperatures fall within the range of simulation results for FL $= 0.1$ to 1. Velocities from larger depths cannot be matched by hydrodynamic simulations in which laser energy is absorbed solely into thermal electrons. However, adding a 50 keV electron tail, as suggested by the observations of hot protons, improves agreement.

The authors thank B. K. F. Young, R. Shepherd, W. H. Goldstein, R. M. More, R. E. Stewart, and R. S. Walling for helpful discussions, and J. Bonlie for technical assistance. This work was performed under the auspices of the U.S. Department of Energy by the Lawrence Livermore National Laboratory under Contract No. W-7405-Eng-48.

[1] D. Strickland and G. Mourou, Opt. Commun. **56**, 219 (1985).
[2] R. M. More *et al.,* J. Phys. (Paris), Colloq. **49**, C7-43 (1988).
[3] A. Ng *et al.,* Phys. Rev. E **51**, 5208 (1995).
[4] H. M. Milchberg *et al.,* Phys. Rev. Lett. **61**, 2364 (1988).
[5] D. F. Price *et al.,* Phys. Rev. Lett. **75**, 252 (1995).
[6] J. C. Kieffer *et al.,* Phys. Fluids B **5**, 2676 (1993).
[7] J. D. Lindl *et al.,* Phys. Today **45**, No. 9, 32 (1992).
[8] See, for example, special issue on *Radiative Properties of Hot Dense Matter,* edited by R. W. Lee [J. Quant. Spectrosc. Radiat. Transf. **54** (1995)].
[9] U. Teubner *et al.,* Phys. Plasmas **2**, 972 (1995).
[10] P. Audebert *et al.,* J. Phys. B **27**, 3303 (1994).
[11] P. Audebert *et al.,* Europhys. Lett. **19**, 189 (1992).
[12] Z. Jiang *et al.,* Phys. Plasmas **2**, 1702 (1995).
[13] H. Chen *et al.,* Phys. Rev. Lett. **70**, 3431 (1993).
[14] A. Rousse *et al.,* Phys. Rev. E **50**, 2200 (1994).
[15] D. D. Meyerhofer *et al.,* Phys. Fluids B **5**, 2584 (1993).
[16] S. J. Gitomer *et al.,* Phys. Fluids **29**, 2679 (1986).
[17] A. P. Fews *et al.,* Phys. Rev. Lett. **73**, 1801 (1994).
[18] R. Shepherd *et al.,* in *Proceedings of X-ray and UV Detectors,* SPIE Proceedings Vol. 2278 (SPIE–International Society for Optical Engineering, Bellingham, WA, 1994), p. 78.
[19] H. M. Milchberg and R. R. Freeman, Phys. Rev. A **41**, 2211 (1990).
[20] B.-T. V. Vu *et al.,* Phys. Rev. Lett. **72**, 3823 (1994).
[21] X. Liu and D. Umstadter, Phys. Rev. Lett. **69**, 1935 (1992).
[22] G. B. Zimmerman and W. L. Kruer, Comments Plasma Phys. Controlled Fusion **II**, 51 (1975).
[23] J. D. Bonlie *et al.,* in *Proceedings on Generation, Amplification, and Measurement of Ultrashort Laser Pulses,* SPIE Proceedings Vol. 2116 (SPIE–International Society for Optical Engineering, Bellingham, WA, 1994), p. 312.
[24] W. E. White *et al.,* Opt. Lett. **17**, 1067 (1992).
[25] G. Guethlein *et al.,* Rev. Sci. Instrum. **66**, 333 (1995).
[26] E. Alley, in LLNL Report No. 160-165, 1992.
[27] M. E. Foord *et al.* (to be published).
[28] Y. T. Lee and R. M. More, Phys. Fluids **27**, 1273 (1984).
[29] J. Delettrez, Can. J. Phys. **64**, 932 (1986).
[30] M. K. Prasad and D. S. Kershaw, Phys. Fluids B **1**, 2430 (1989).
[31] J. P. Matte *et al.,* Phys. Rev. Lett. **53**, 1461 (1984).